Supplementary Figures and Legends

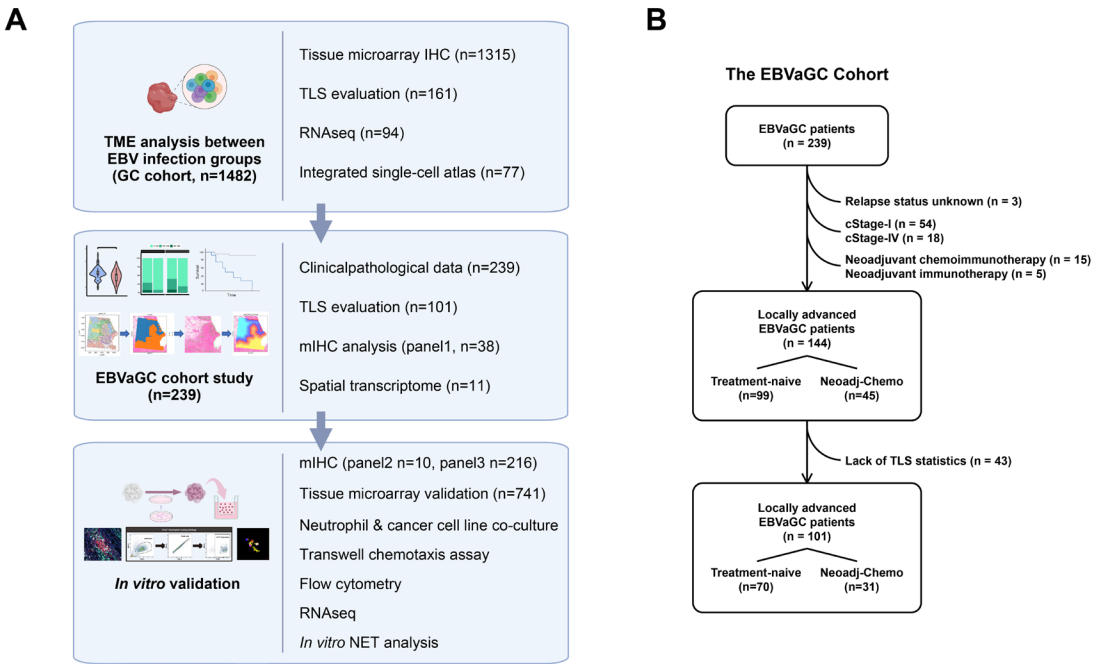

Supplementary Figure 1. Study design and Cohort collection

A. The overview of the study (Created in BioRender. Bi, J. (2026) https://BioRender.com/c8ts4i2).

B. The selection process of the EBVaGC cohort.

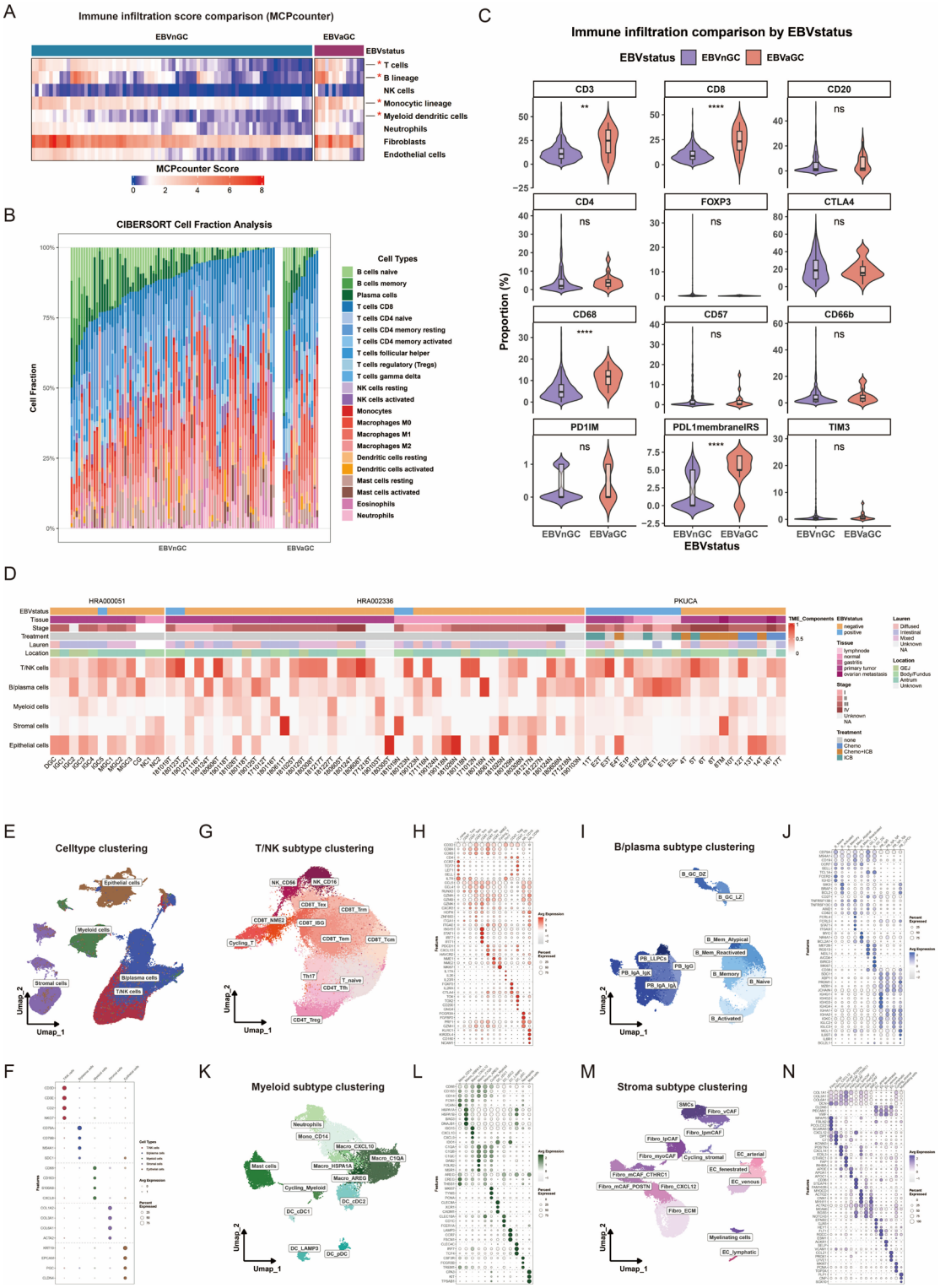

Supplementary Figure 2. Immune infiltration landscape and the integrated single-cell atlas of EBVaGC

A. Heatmap displaying the microenvironmental component scores for each sample (n=94) based on MCPcounter analysis. (two-sided Wilcoxon rank-sum test; ns, P≥0.05; *P<0.05; **P<0.01; ***P<0.001). Exact P values are shown in Source Data.

B. Stacked bar chart showing the deconvoluted abundance of 21 cell types calculated by the Cibersort algorithm (n=94).

C. Comparison of immune infiltration between EBVaGC (n=17) and EBVnGC (n=550) tumors based on tissue microarray immunohistochemical staining scores. (two-sided Wilcoxon rank-sum test). Exact P values are shown in Source Data.

D. Complex heatmap showing the clinical pathological grouping information and the proportion of primary cell types across integrated single-cell atlas samples (n=77).

E-F. Major cell types in the integrated single-cell atlas (n=77). (E) UMAP plot and (F) dot plot for features

G-N. Cell subtypes in the integrated single-cell atlas (n=77). (G) T and NK cell subtypes and (H) their features, (I) B and plasma cell subtypes and (J) their features, (K) myeloid cell subtypes and (L) their features, (M) stromal cell subtypes and (N) their features.

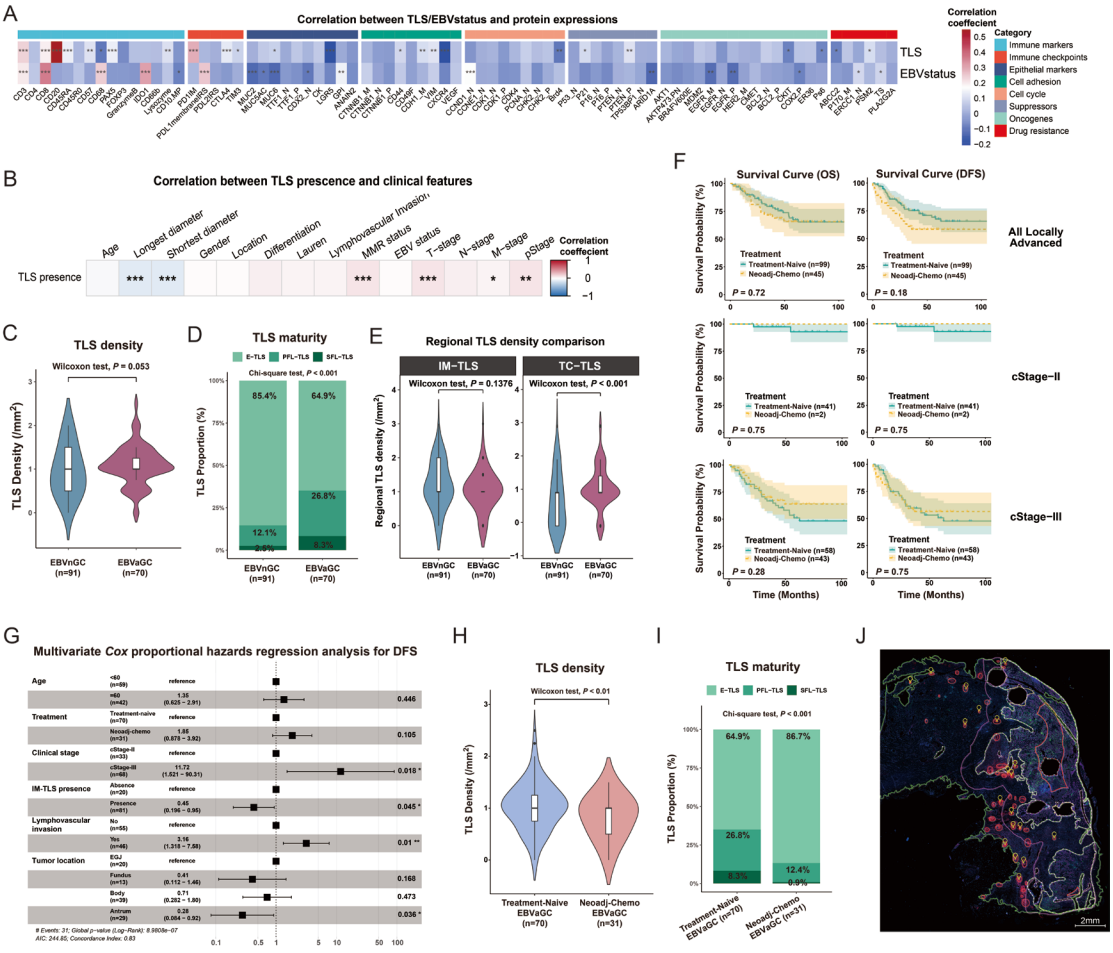

Supplementary Figure 3. Correlation analysis between TLS presence, clinical features, and the impact of neoadjuvant chemotherapy on TLS in gastric cancer

A. Heatmap showing correlations between TLS presence or EBV status and IHC-based protein marker scores (tissue microarray cohort, n=741; Pearson's correlation). *P<0.05, **P<0.01, ***P<0.001. Exact P values in Source Data.

B. Heatmap showing correlations between TLS presence and clinicopathological factors (tissue microarray cohort, n=741; point-biserial for continuous variables; Cramér's V for categorical variables). Exact P values in Source Data.

C. Violin plot comparing overall TLS density between EBVnGC and EBVaGC (two-sided Wilcoxon rank-sum test). Exact P values in Source Data.

D. Stacked bar chart comparing TLS maturation stage proportions between EBVnGC and EBVaGC (two-sided Chi-square test). E-TLS: early TLS; PFL-TLS: primary follicular-like TLS; SFL-TLS: secondary follicular-like TLS. Exact P values in Source Data.

E. Violin plots comparing IM-TLS and TC-TLS regional density between EBVnGC and EBVaGC (two-sided Wilcoxon rank-sum test). Exact P values in Source Data.

F. Kaplan-Meier curves comparing OS and DFS between Treatment-Naive and Neoadj-Chemo groups, stratified by clinical stage (All Locally Advanced, cStage-II, cStage-III).

G. Forest plot of multivariate Cox regression for DFS, including age, treatment, clinical stage, IM-TLS presence, lymphovascular invasion, and tumor location.

H. Violin plot comparing TLS density between treatment-naive and Neoadj-Chemo EBVaGC patients (two-sided Wilcoxon rank-sum test). Exact P values in Source Data.

I. Stacked bar chart of TLS maturation stage proportions between treatment-naive and Neoadj-Chemo EBVaGC patients (two-sided Chi-square test). Exact P values in Source Data.

J. Representative mIHC schematic of the invasive margin (n=38): white dashed line, tumor border; red/purple lines, isoclines ±1 mm from the border, defining the invasive margin. Red circles and yellow pins mark TLS structures.

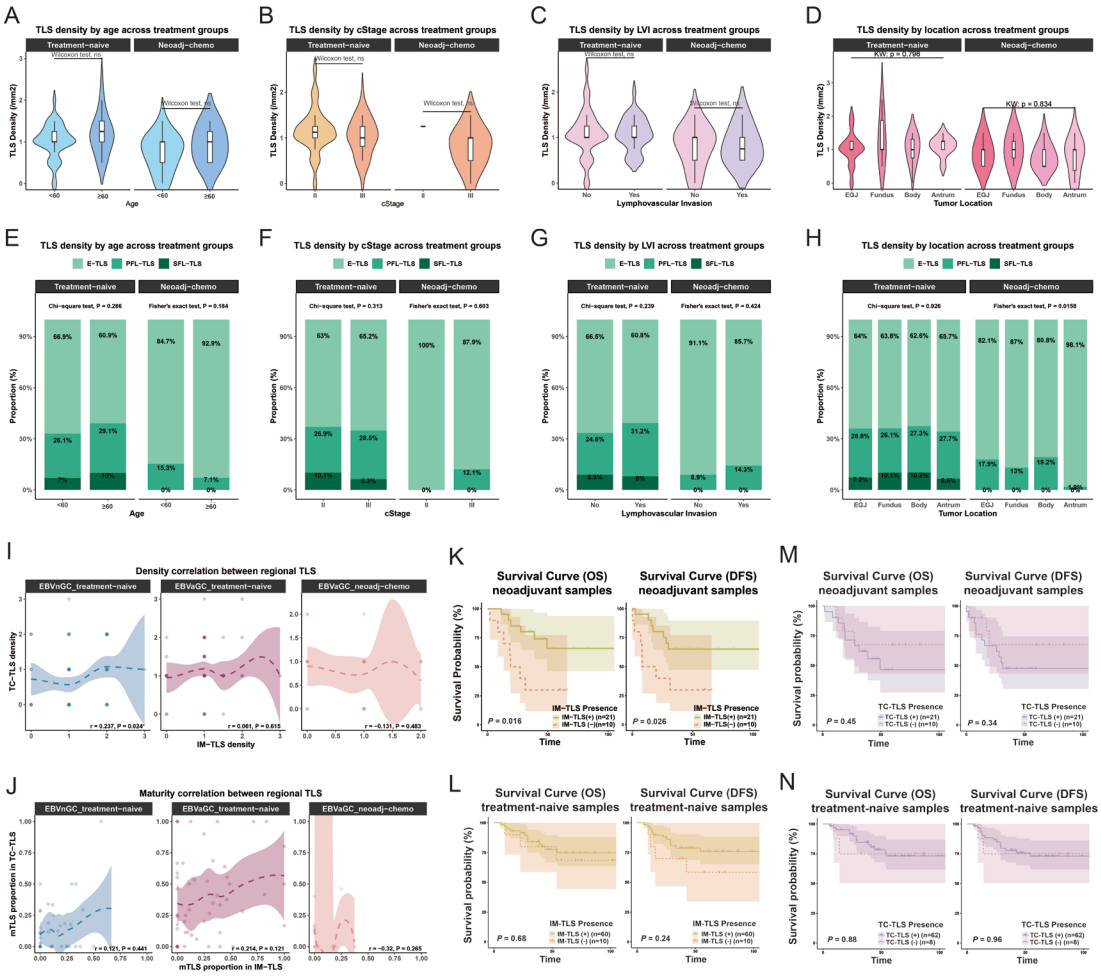

Supplementary Figure 4. Correlation analysis of regional TLS with clinical pathological factors and prognostic analysis

A-D. Violin plot showing TLS density differences between treatment groups (n=101) among (A) age, (B) clinical stage, (C) lymphovascular invasion, and (D) tumor location groups, two-sided Wilcoxon rank-sum test for (A-C) and Kruskal-Wallis H test for (D), ns $P \geq 0.05$, *P<0.05, **P<0.01, ***P<0.001. Exact P values in Source Data.

E-H. Stacked bar chart showing TLS density differences between treatment groups(n=101) among (E) age, (F) clinical stage, (G) lymphovascular invasion, and (H) tumor location groups (two-sided Chi-square test or Fisher's exact test). Exact P values in Source Data.

I-J. Spearman correlation analysis between (I) IM-TLS density and TC-TLS density or (J) the mature ratio of IM-TLS and the mature ratio of TC-TLS in treatment-naïve EBVnGC (n=91), treatment-naïve EBVaGC (n=70), and EBVaGC receiving

neoadjuvant chemotherapy (n=31) (from left to right).

K-N Survival analysis stratified by (K) the presence of IM-TLS in EBVaGC receiving neoadjuvant chemotherapy, (L) the presence of IM-TLS in treatment-naive EBVaGC, (M) the presence of TC-TLS in EBVaGC receiving neoadjuvant chemotherapy, and (N) the presence of TC-TLS in treatment-naive EBVaGC.

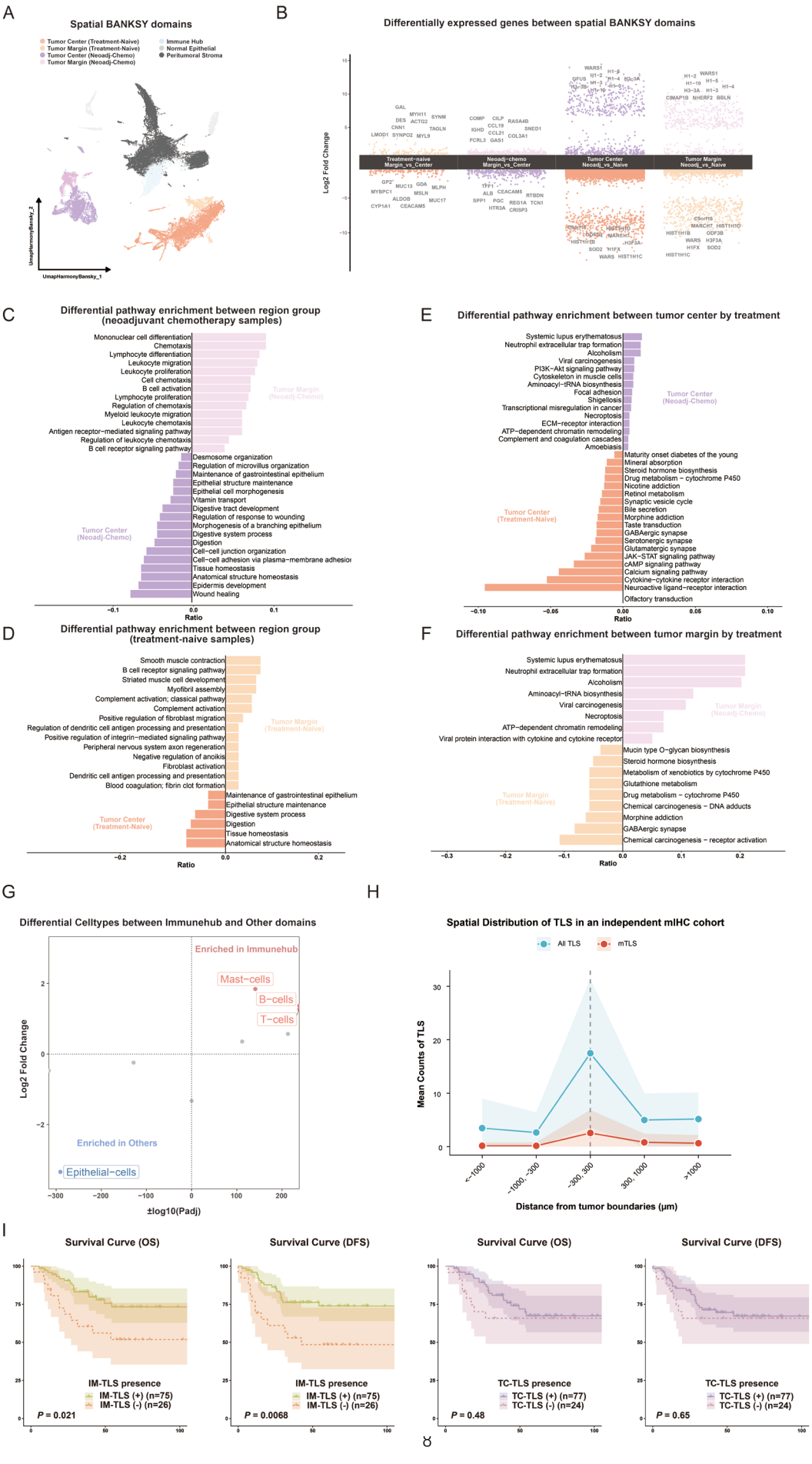
A
Spatial BANKSY domains
Tumor Center (Treatment-Naive)
Tumor Margin (Treatment-Naive)
Tumor Center (Neoadj-Chemo)
Tumor Margin (Neoadj-Chemo)
Immune Hub
Normal Epithelial
Peritumoral Stroma
UmapHarmonyBansky_2
UmapHarmonyBansky_1
B
Differentially expressed genes between spatial BANKSY domains
Log2 Fold Change
Treatment−naive Margin_vs_Center
Neoadj−chemo Margin_vs_Center
Tumor Center Neoadj_vs_Naive
Tumor Margin Neoadj_vs_Naive
C
Differential pathway enrichment between region group (neoadjuvant chemotherapy samples)
Mononuclear cell differentiation
Chemotaxis
Lymphocyte differentiation
Leukocyte migration
Leukocyte proliferation
Cell chemotaxis
B cell activation
Lymphocyte proliferation
Regulation of chemotaxis
Myeloid leukocyte migration
Leukocyte chemotaxis
Antigen receptor−mediated signaling pathway
Regulation of leukocyte chemotaxis
B cell receptor signaling pathway
Tumor Margin (Neoadj-Chemo)
Desmosome organization
Regulation of microvillus organization
Maintenance of gastrointestinal epithelium
Epithelial structure maintenance
Epithelial cell morphogenesis
Vitamin transport
Digestive tract development
Regulation of response to wounding
Morphogenesis of a branching epithelium
Digestive system process
Digestion
Cell−cell junction organization
Cell−cell adhesion via plasma−membrane adhesio
Tissue homeostasis
Anatomical structure homeostasis
Epidermis development
Wound healing
Tumor Center (Neoadj-Chemo)
Ratio
D
Differential pathway enrichment between region group (treatment-naive samples)
Smooth muscle contraction
B cell receptor signaling pathway
Striated muscle cell development
Myofibril assembly
Complement activation; classical pathway
Complement activation
Positive regulation of fibroblast migration
Regulation of dendritic cell antigen processing and presentation
Positive regulation of integrin−mediated signaling pathway
Peripheral nervous system axon regeneration
Negative regulation of anoikis
Fibroblast activation
Dendritic cell antigen processing and presentation
Blood coagulation; fibrin clot formation
Tumor Margin (Treatment-Naive)
Maintenance of gastrointestinal epithelium
Epithelial structure maintenance
Digestive system process
Digestion
Tissue homeostasis
Anatomical structure homeostasis
Tumor Center (Treatment-Naive)
Ratio
E
Differential pathway enrichment between tumor center by treatment
Systemic lupus erythematosus
Neutrophil extracellular trap formation
Alcoholism
Viral carcinogenesis
PI3K−Akt signaling pathway
Cytoskeleton in muscle cells
Aminoacyl−tRNA biosynthesis
Focal adhesion
Shigellosis
Transcriptional misregulation in cancer
Necroptosis
ECM−receptor interaction
ATP−dependent chromatin remodeling
Complement and coagulation cascades
Amoebiasis
Tumor Center (Neoadj-Chemo)
Maturity onset diabetes of the young
Mineral absorption
Steroid hormone biosynthesis
Drug metabolism − cytochrome P450
Nicotine addiction
Retinol metabolism
Synaptic vesicle cycle
Bile secretion
Morphine addiction
Taste transduction
GABAergic synapse
Serotonergic synapse
Glutamatergic synapse
JAK−STAT signaling pathway
cAMP signaling pathway
Calcium signaling pathway
Cytokine−cytokine receptor interaction
Neuroactive ligand−receptor interaction
Olfactory transduction
Tumor Center (Treatment-Naive)
Ratio
F
Differential pathway enrichment between tumor margin by treatment
Systemic lupus erythematosus
Neutrophil extracellular trap formation
Alcoholism
Aminoacyl−tRNA biosynthesis
Viral carcinogenesis
Necroptosis
ATP−dependent chromatin remodeling
Viral protein interaction with cytokine and cytokine receptor
Tumor Margin (Neoadj-Chemo)
Mucin type O−glycan biosynthesis
Steroid hormone biosynthesis
Metabolism of xenobiotics by cytochrome P450
Glutathione metabolism
Drug metabolism − cytochrome P450
Chemical carcinogenesis − DNA adducts
Morphine addiction
GABAergic synapse
Chemical carcinogenesis − receptor activation
Tumor Margin (Treatment-Naive)
Ratio
G
Differential Celltypes between Immunehub and Other domains
Enriched in Immunehub
Mast−cells
B−cells
T−cells
Enriched in Others
Epithelial−cells
Log2 Fold Change
±log10(Padj)
H
Spatial Distribution of TLS in an independent mIHC cohort
All TLS
mTLS
Mean Counts of TLS
<−1000
−1000, −300
−300, 300
300, 1000
>1000
Distance from tumor boundaries (μm)
I
Survival Curve (OS)
IM-TLS presence
IM-TLS (+) (n=75)
IM-TLS (-) (n=26)
P = 0.021
Survival Curve (DFS)
IM-TLS presence
IM-TLS (+) (n=75)
IM-TLS (-) (n=26)
P = 0.0068
Survival Curve (OS)
TC-TLS presence
TC-TLS (+) (n=77)
TC-TLS (-) (n=24)
P = 0.48
Survival Curve (DFS)
TC-TLS presence
TC-TLS (+) (n=77)
TC-TLS (-) (n=24)
P = 0.65

Supplementary Figure 5. Characterization of spatial BANKSY niche domains and functional validation of the redefined invasive margin

A. UMAP visualization illustrating the clustering of distinct spatial BANKSY niche domains across all 11 spatial transcriptomic samples.

B. Scatter plots detailing the DEGs among specific BANKSY niche domains. Comparisons are shown for spatial regions (Margin vs. Center) and treatment modalities (Neoadjuvant chemotherapy (n=6) vs. Treatment-naïve (n=5)).

C-F. Bar plots displaying differential pathway enrichment analyses. Comparisons are made between the tumor center and tumor margin spots in (C) neoadjuvant chemotherapy-treated (n=6) and (D) treatment-naïve (n=5) EBVaGC samples. Additionally, treatment-induced pathway alterations (Neoadjuvant chemotherapy vs. Treatment-naïve) are evaluated within (E) the tumor center and (F) the tumor margin spots.

G. Volcano plot highlighting the differential abundance of cell types between the immune hub domain and other domains of all 11 spatial transcriptomic samples. Immune cells (Mast cells, B cells, and T cells) are significantly enriched in the immune hub, whereas epithelial cells are enriched in other domains.

H. Line plot illustrating the spatial distribution of total TLSs and mature TLSs across various distances from the tumor boundary in an independent multiplex immunohistochemistry cohort (n=23), demonstrating a peak distribution within the redefined ±300 μm zone.

I. Kaplan-Meier survival curves for overall survival and disease-free survival, stratified by the presence or absence of IM-TLS or TC-TLS in the EBVaGC cohort (log-rank test). Notably, the IM here is functionally redefined as ±300 μm from the tumor boundary based on the aforementioned spatial transcriptome and mIHC data.

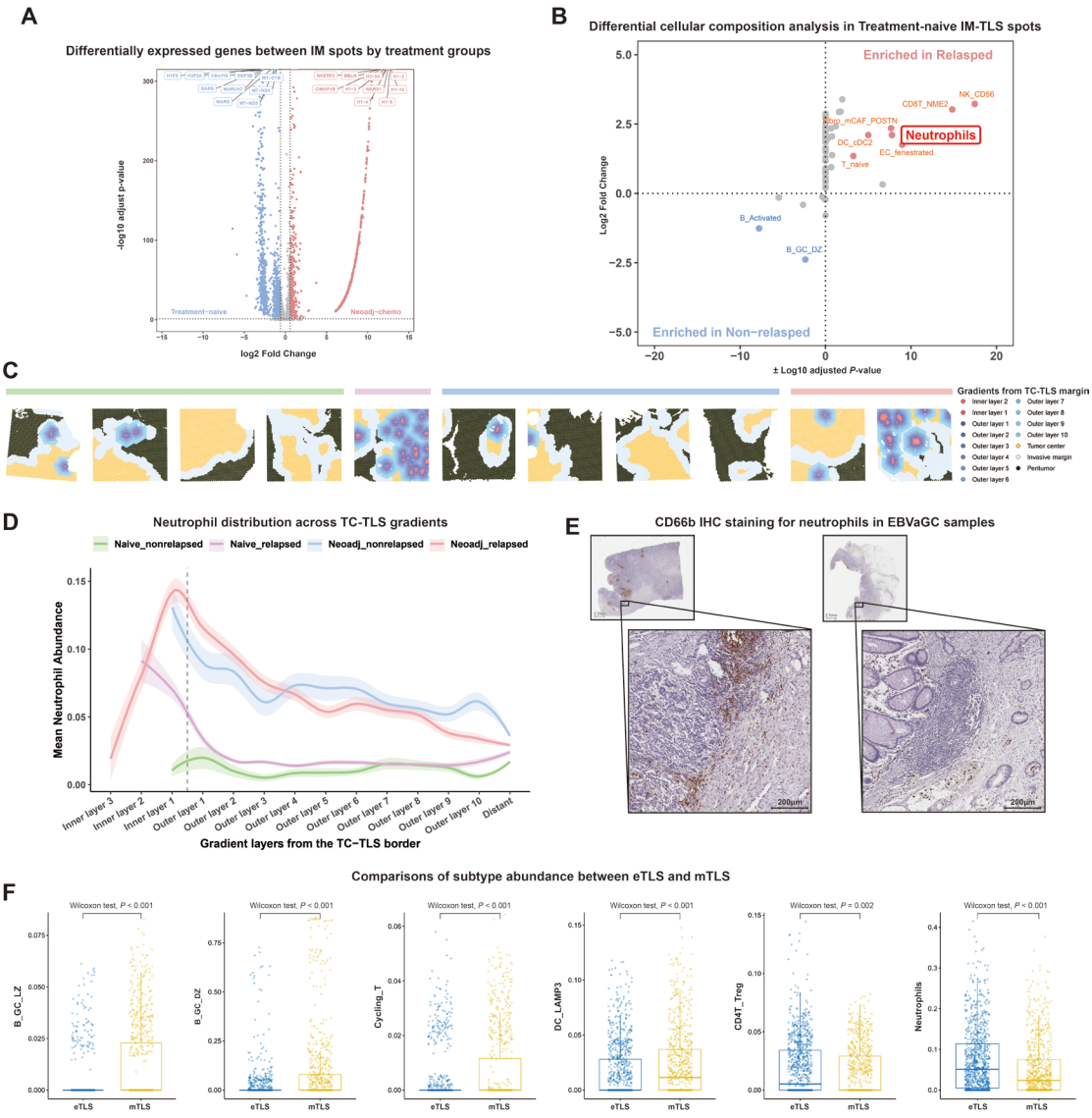

Supplementary Figure 6. Neutrophil Infiltration affects TLS formation and maturation.

A. Volcano plot illustrating the DEGs in the IM spots between different treatment groups (Neoadjuvant chemotherapy (n=6) vs. Treatment-naïve(n=5)).

B. Differential cellular composition analysis of IM-TLS spots between relapsed (n=1) and non-relapsed (n=4) groups within the treatment-naïve EBVaGC cohort. (Red highlight indicates neutrophils enriched in the relapsed group).

C. Spatial transcriptomics visualizations (n=11) depicting the defined spatial gradient layers along the tumor center TLS (TC-TLS) margins.

D. Comparison of mean neutrophil abundance along the TC-TLS margin gradients across four distinct treatment and prognosis groups, including treatment-naïve non-

relapsed samples (n=4), treatment-naïve relapsed samples (n=1), neoadjuvant chemotherapy non-relapsed samples (n=4), neoadjuvant chemotherapy relapsed samples (n=2).

E. Representative immunohistochemical staining of CD66b in EBVaGC samples (n=36), showing abundant $CD66b^{+}$neutrophil infiltration at the periphery of an immature lymphoid aggregate (left) and its absence around a mature TLS (right).

F. Boxplots comparing the abundances of various TLS-related cellular subtypes and neutrophils between early/immature TLS (eTLS) and mature TLS (mTLS) spots of all 11 spatial transcriptomic samples (two-sided Wilcoxon rank-sum test, ns $P \geq 0.05$, *P<0.05, **P<0.01, ***P<0.001). Exact P values in Source Data.

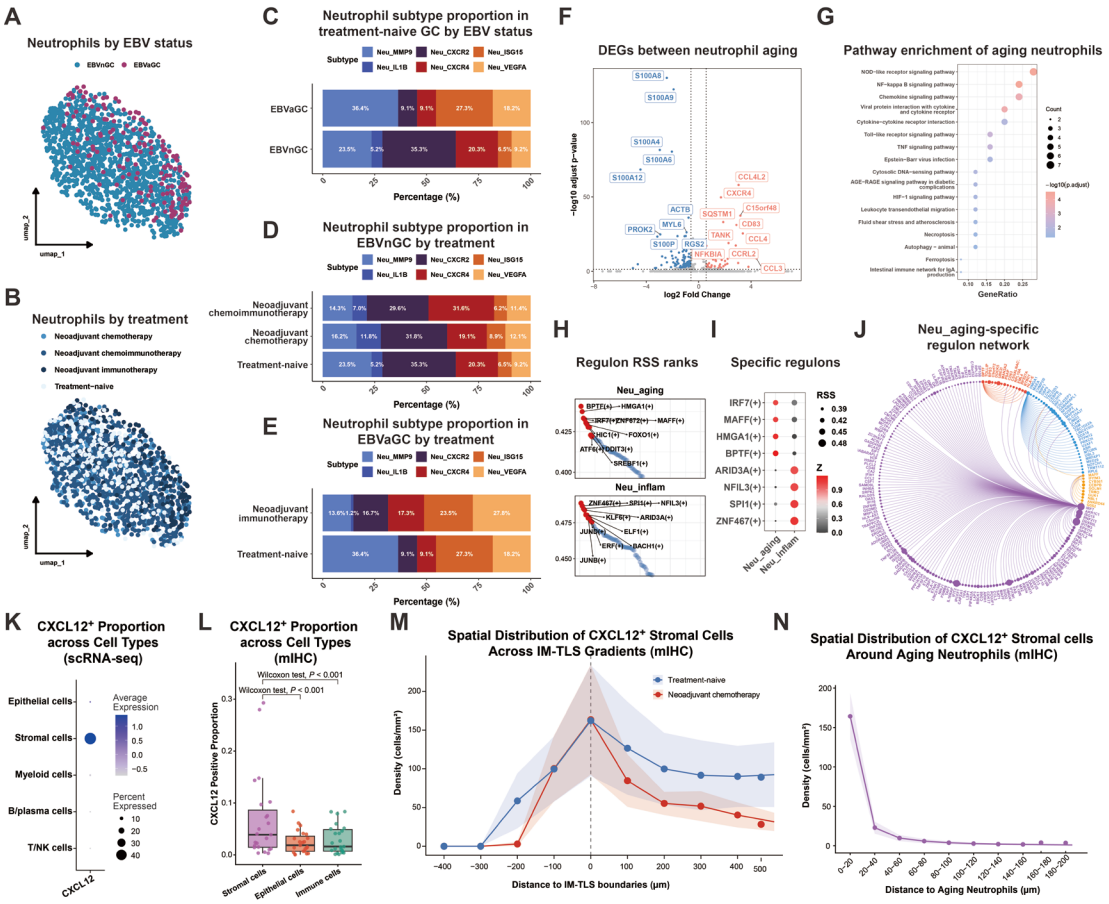

Supplementary Figure 7. Characterization of aging neutrophil phenotype and functional validation

A-B. UMAP embeddings showing the distribution of neutrophils colored by (A) EBV infection status (EBVnGC n=17, EBVaGC n=4) and (B) treatment modality (treatment-naive n=11, neoadjuvant chemotherapy n=3, neoadjuvant chemoimmunotherapy n=5, neoadjuvant immunotherapy n=2).

C-E. Stacked bar charts showing the compositional proportions of neutrophil subtypes across different clinical scenarios: (C) between EBVaGC (n=9) and EBVnGC (n=2) in treatment-naïve samples; (D) across different treatment groups (treatment-naive n=9, neoadjuvant chemotherapy n=3, neoadjuvant chemoimmunotherapy n=5) in EBVnGC samples; and (E) across different treatment groups (treatment-naive n=2, neoadjuvant immunotherapy n=2) in EBVaGC samples.

F. Volcano plot highlighting DEGs between the aging (Neu_aging) and inflammatory (Neu_inflam) neutrophil subtypes (n=21).

G. Bubble plot illustrating KEGG pathway enrichment analysis of genes upregulated

in aging neutrophils (n=21).

H-I. Transcription factor (regulon) activity analysis (SCENIC) comparing Neu_aging and Neu_inflam subtypes, showing (H) the top rank-sum (RSS) regulons and (I) a dot plot of specific key regulons for both subtypes (n=21).

J. Circos plot displaying the transcriptional regulatory network of aging neutrophil-specific regulons (n=21).

K. Dot plot displaying the average expression and expression percentage of CXCL12 across diverse microenvironmental cell types based on scRNA-seq data (n=77).

L. Boxplots comparing the proportion of $CXCL12^{+}$cells among stromal, epithelial, and immune cell populations, validated in an independent mIHC cohort (n=23) (two-sided Wilcoxon rank-sum test). Exact P values in Source Data.

M. Line plot comparing the spatial density distribution of $CXCL12^{+}$stromal cells across the IM-TLS gradient (from the tumor center towards the peritumoral stroma) between treatment-naïve (n=5) and neoadjuvant chemotherapy (n=18) samples.

N. Line plot illustrating the spatial density of $CXCL12^{+}$stromal cells at varying distances from aging neutrophils based on spatial mIHC analysis (n=23).

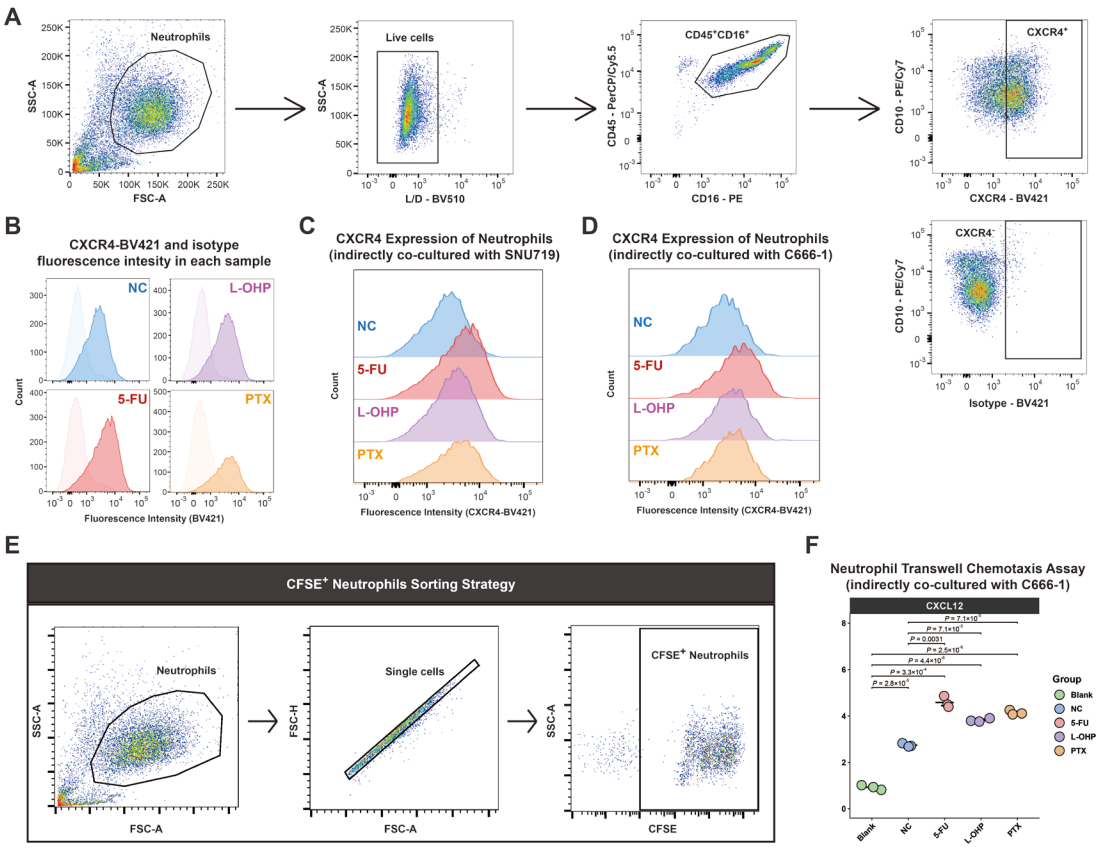

Supplementary Figure 8. Flow cytometry gating strategies and isotype controls for neutrophil CXCR4 expression.

A. Comprehensive gating strategy for identifying $CXCR4^{+}$neutrophils. Cells were sequentially gated by morphology (FSC/SSC), viability (Live cells, L/D-), and neutrophil lineage markers ($CD45^{+}CD16^{+}$). The appropriate BV421 isotype control was used to establish the threshold for CXCR4 positivity.

B. Representative flow cytometry histograms demonstrating CXCR4-BV421 fluorescence intensity (colored peaks) overlaid with their respective isotype controls (light shaded peaks) across different treatment groups (NC, 5-FU, L-OHP, PTX) (n=3).

C-D. Representative flow cytometry histograms analyzing the CXCR4 expression on neutrophils indirectly co-cultured with (C) SNU719 (n=3) or (D) C666-1 (n=3) cell lines, following pretreatment with various chemotherapeutic agents (NC, 5-FU, L-OHP, and PTX).

E. Flow cytometry gating strategy for isolating CFSE-labeled neutrophils. Cells were sequentially gated by morphology (FSC/SSC), doublet discrimination (Single cells,

FSC-A/FSC-H), and CFSE positivity.

F. Transwell migration assay evaluating the chemotactic effect of CXCL12 on neutrophils indirectly co-cultured with the C666-1 cell line across different treatment groups (n=3 for each group). (two-sided Student's t-test with Bonferroni correction for multiple comparisons; ** $P < 0.01$; *** $P < 0.001$).

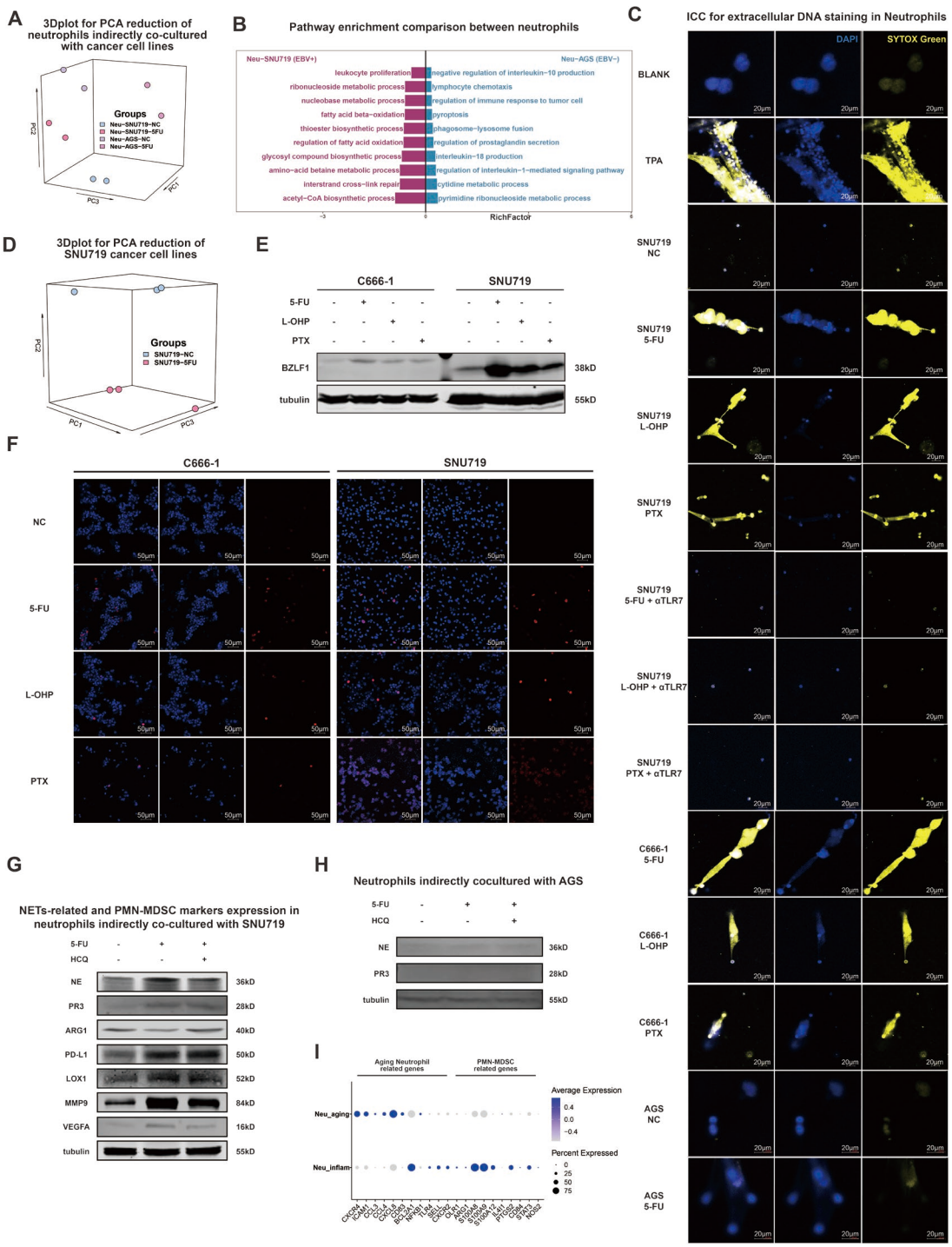

175

176 **Supplementary Figure 9. Functional validation of chemotherapy-induced EBV**
177 **reactivation, NET formation, and phenotypic shifts *in vitro***

178 A. Three-dimensional Principal Component Analysis (3D-PCA) plot based on RNA-
179 seq data, illustrating the overall transcriptomic variance among human primary
180 neutrophils indirectly co-cultured with distinct cancer cell lines (SNU719 (n=4) vs.
181 AGS (n=4)) under 5-FU treatment or control conditions.

B. Bidirectional bar chart comparing the Gene Ontology (GO) biological process (BP) pathway enrichments between 5-FU-treated neutrophils indirectly co-cultured with SNU719 (EBV+, n=4) versus AGS (EBV-, n=4) cell lines.

C. Representative immunocytochemistry (ICC) images visualizing extracellular DNA release (NET formation) in primary neutrophils under various experimental conditions (n=3 for each group). Nuclei were counterstained with DAPI (blue), and extracellular DNA was detected by SYTOX Green (yellow). Treatments included TPA (positive control), conditioned media from various cell lines (SNU719, C666-1, AGS) treated with different chemotherapeutic agents (5-FU, L-OHP, PTX), and the addition of an anti-TLR7 neutralizing antibody (αTLR7). Scale bar, 20 μm.

D. 3D-PCA plot demonstrating the distinct transcriptomic clustering of SNU719 cancer cell lines before (n=3) and after (n=3) 5-FU treatment.

E. Western blot analysis (n=3) detecting the expression of the key EBV reactivation transcription factor, BZLF1, in EBV-positive cell lines (C666-1 and SNU719) following exposure to diverse chemotherapeutic agents (5-FU, L-OHP, PTX). Tubulin served as the loading control.

F. Representative immunofluorescence images (n=3 for each group) validating EBV lytic reactivation in C666-1 and SNU719 cell lines treated with 5-FU, L-OHP, or PTX. BZLF1 expression is shown in red, and nuclei are stained with DAPI (blue). Scale bar, 50 μm.

G. Western blot analysis (n=3) evaluating the protein expression of NET-related markers (NE, PRR3) and PMN-MDSC markers (ARG1, PD-L1, LOX1, MMP9, VEGFA) in neutrophils indirectly co-cultured with SNU719. Neutrophils were pretreated with or without hydroxychloroquine (HCQ, a TLR inhibitor) prior to co-culture with 5-FU-treated SNU719 cells. Tubulin served as the loading control.

H. Western blot analysis (n=3) of NET-associated molecules (NE, PR3) in control neutrophils indirectly co-cultured with the EBV-negative cell line AGS, with or without 5-FU and HCQ treatments. Tubulin served as the loading control.

I. Dot plot validating the specific expression profiles of aging neutrophil-related genes

and PMN-MDSC-related genes between the defined Neu_aging and Neu_inflam subtypes based on single-cell RNA sequencing data (n=21).

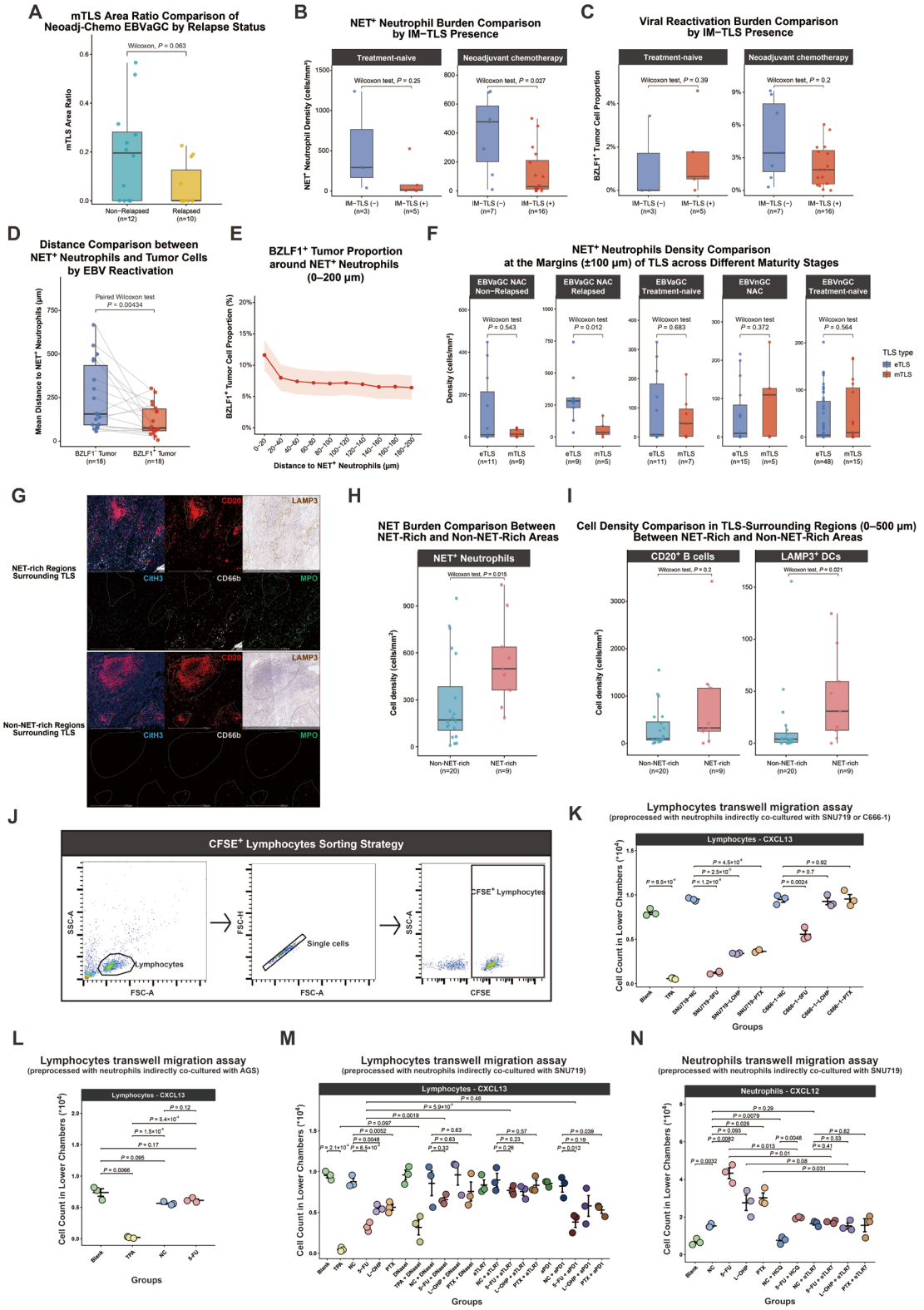

Supplementary Figure 10. Spatial clinical evaluations of TLS/NETs/EBV reactivation and in vitro validations of neutrophil-lymphocyte chemotaxis

A. mTLS area ratio in non-relapsed versus relapsed patients within the neoadjuvant chemotherapy-treated EBVaGC cohort (two-sided Wilcoxon rank-sum test).

B-C. (B) NET^+ neutrophil density and (C) viral reactivation burden ($BZLF1^+$ tumor cell proportion) compared between IM-TLS(-) and IM-TLS(+) patients, stratified by treatment-naïve and neoadjuvant chemotherapy groups (two-sided Wilcoxon rank-sum test).

D. Mean spatial distance from NET^+ neutrophils to $BZLF1^-$ versus $BZLF1^+$ tumor cells (paired Wilcoxon test).

E. Spatial distribution of $BZLF1^+$ tumor cell proportion at increasing distances (0-200 μm) from NET^+ neutrophils (n=23).

F. NET^+ neutrophil density at eTLS versus mTLS margins (±100 μm) across five cohorts: EBVaGC NAC non-relapsed/relapsed, EBVaGC treatment-naïve, EBVnGC NAC, and EBVnGC treatment-naïve (two-sided Wilcoxon rank-sum test).

G. Representative images (n=23) showing morphological differences between NET-rich and non-NET-rich regions surrounding TLS, with $CD20^+$ B cell and $LAMP3^+$ DC entrapment evident only in NET-rich areas.

H. NET^+ neutrophil density in manually annotated NET-rich versus non-NET-rich regions (Wilcoxon signed-rank test).

I. $CD20^+$ B cell and $LAMP3^+$ DC density within 0-500 μm of TLS in NET-rich versus non-NET-rich regions, from serial IHC sections (Wilcoxon signed-rank test).

J. Flow cytometry gating strategy for CFSE-labeled lymphocytes (morphology, doublet discrimination, CFSE positivity).

K-M. Transwell migration assays (n=3 for each group) assessing CFSE-labeled lymphocyte chemotaxis toward CXCL13 after preconditioning with conditioned media from neutrophils co-cultured with (K) SNU719 or C666-1, (L) AGS, or (M) SNU719 under indicated treatments (5-FU, L-OHP, PTX, DNase I, αTLR7, αPD1).

N. Transwell migration assay (n=3 for each group) of neutrophil chemotaxis toward CXCL12 following co-culture with SNU719 under indicated treatments (chemotherapeutic agents, HCQ, αTLR7).

For K-N: two-sided Student's t-test with Bonferroni correction for multiple comparisons.